Supplemental Information

Rethinking Surface-Layer Parameterization: A Turbulence-Based Framework Without Using Similarity Functions and Its Impacts on Surface–Atmosphere Coupling

Kiran Alapaty[1], Jimy Dudhia[2], Pedro A Jiminez[2], Wei Wang[2], and Temple R Lee[3]

Received: DD Month YEAR/ Accepted: DD Month YEAR/ Published online: DD Month YEAR

© Springer Science + Business Media B. V.

Figures S1 and S2 show site-level diurnal composites for Atlanta and Lewisburg, where the dashed curves represent direct ESTAR–BASE differences rather than urban–rural contrasts. For LH (Figs. S1(a–d)), the scheme effect generally remains small at both sites, with differences typically confined to only a few W m^{-2}. At Atlanta, the dashed line fluctuates weakly around zero in both JAN and JUNE, indicating minimal sensitivity of latent heat exchange to the ESTAR formulation.

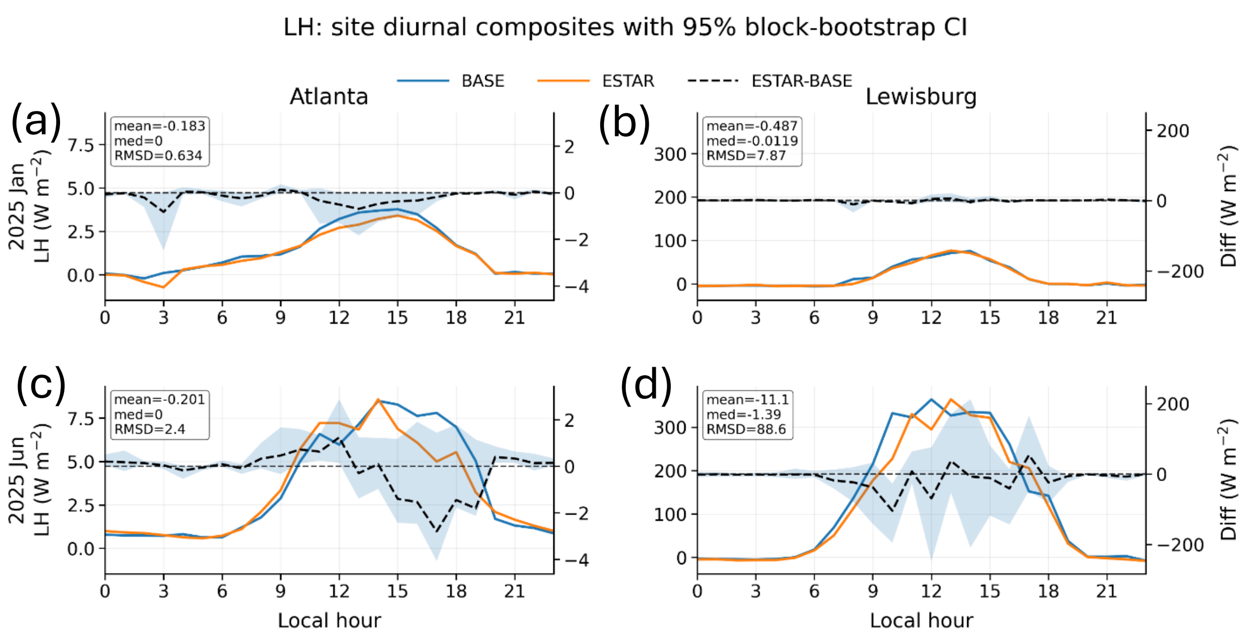

Figure S1 (a-d). Site-level diurnal composites for Atlanta (urban) and Lewisburg (rural) for latent heat flux for January and June.

At Lewisburg, JUNE daytime conditions exhibit somewhat larger fluctuations associated with convective variability, but the response lacks a persistent coherent sign. These results indicate that

LH remains comparatively insensitive to the surface-layer reformulation, consistent with the stronger control of latent heat exchange by moisture availability and land-surface conditions.

In contrast, HFX (Figs. S1(e–h)) exhibits a clearer and more organized daytime response, particularly during JUNE. At Atlanta (Fig. S1 g), ESTAR produces a coherent afternoon reduction

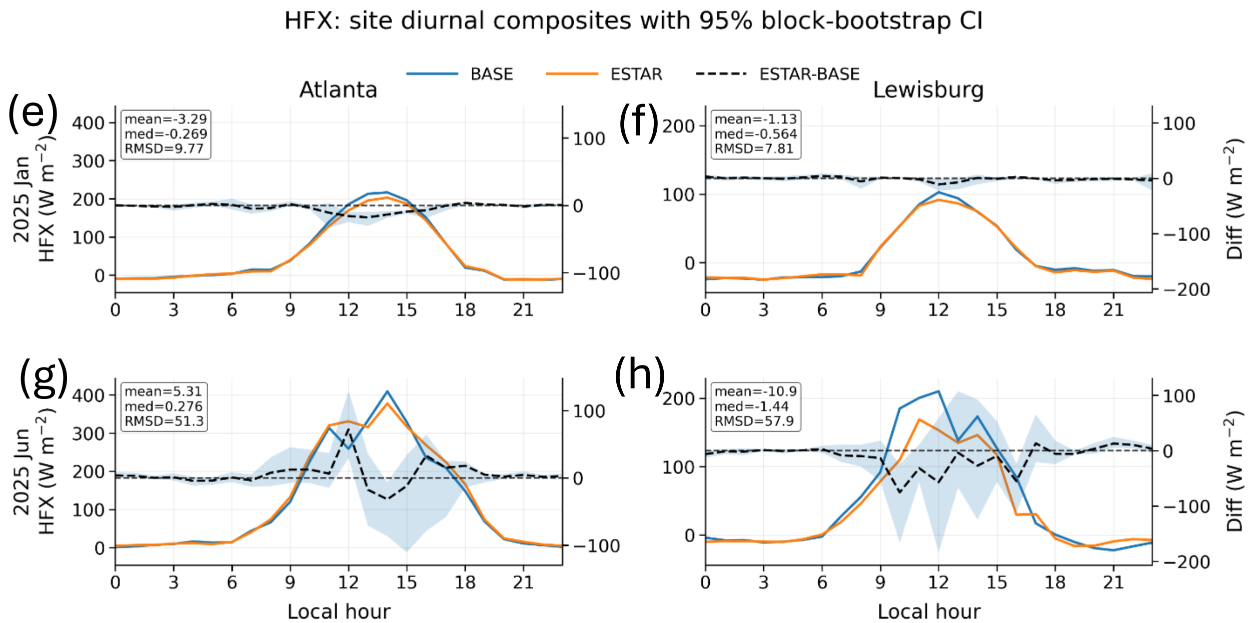

Figure S1 (e-h). Site-level diurnal composites for Atlanta (urban) and Lewisburg (rural) for sensible heat flux for January and June.

in sensible heat flux, with ESTAR–BASE differences reaching approximately −40 to −80 W m^{-2} during peak daytime heating. This indicates that ESTAR modifies the partitioning of surface energy under strongly convective urban conditions. At Lewisburg (Fig. S1 h), the response is weaker but still shows a predominantly negative midday signal, with ESTAR reducing HFX during the primary convective period before differences weaken later in the late afternoon. The largest reductions are generally on the order of several tens of W m^{-2}, although uncertainty (shaded region) increases during periods of strong convective variability. Nevertheless, both sites exhibit their strongest scheme response during daytime convective periods, when buoyancy production and turbulent mixing most actively couple the surface energy balance to boundary-layer evolution. In contrast, nighttime differences remain comparatively small because weak stable-layer turbulence limits the magnitude of turbulent exchange in both formulations.

Figure S2 shows the corresponding site-level composites for u_*. At Atlanta (Fig. S2 c), ESTAR produces a relatively coherent daytime reduction in u_*, with ESTAR–BASE differences generally on the order of −0.05 to −0.15 m s^{-1} during JUNE. At Lewisburg (Fig. S2 d), ESTAR also produces a predominantly negative daytime response, although the signal is more variable and intermittently weakens toward zero during portions of the afternoon. The largest reductions at both sites occur during the convective daytime period, when surface heating and turbulent mixing are strongest. In BASE, turbulent coupling is regulated through empirical MOST stability corrections, whereas in

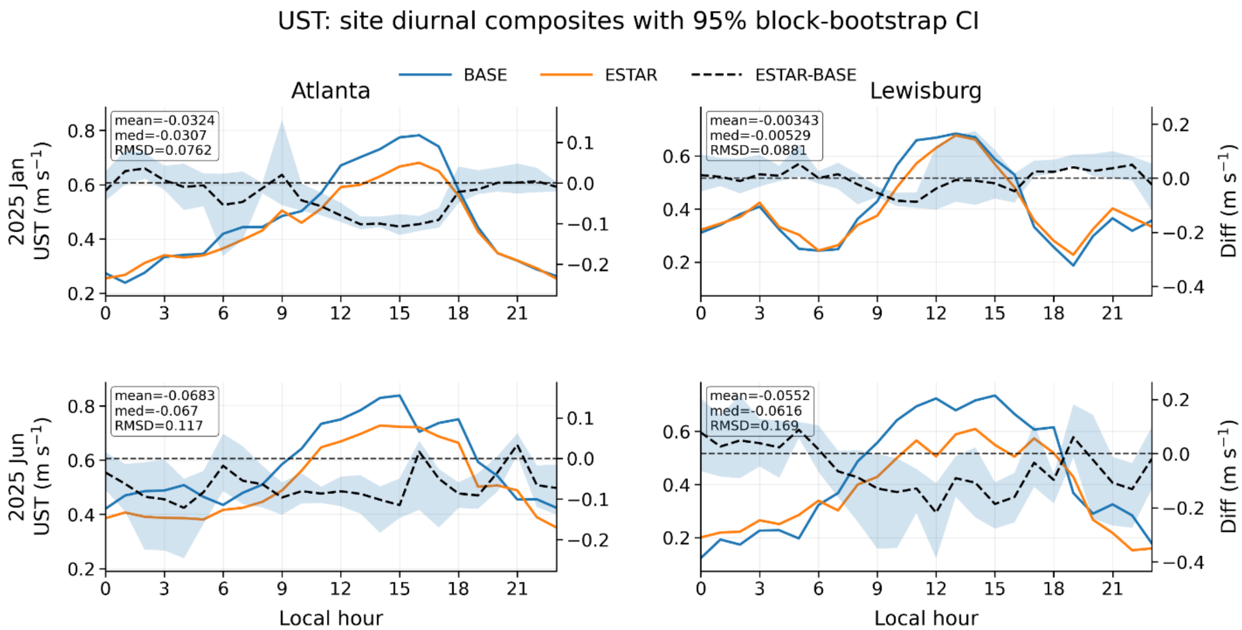

Figure S2. Site-level diurnal composites for Atlanta (urban) and Lewisburg (rural) for friction velocity for January and June.

ESTAR the turbulent velocity scale e_* directly governs the exchange coefficients. Consequently, the differences shown here reflect contrasting representations of shear–buoyancy coupling and turbulent transport between the two formulations. The urban site exhibits the most coherent and persistent response during summer conditions, indicating greater sensitivity of urban turbulent exchange to the alternative turbulence scaling used in ESTAR.

Overall, the site-level composites indicate that ESTAR produces its clearest and most physically coherent responses in sensible heat exchange and turbulent coupling during daytime convective conditions, when buoyancy production and turbulent mixing most actively couple the surface energy balance to boundary-layer evolution. In contrast, latent heat flux remains comparatively weakly affected, indicating stronger control by moisture availability and land-surface conditions. The stronger and more systematic response over Atlanta further suggests that the turbulence-based ESTAR formulation interacts more strongly with urban surface heating, roughness, and buoyancy production, while the similarity-function-based BASE formulation produces comparatively weaker sensitivity to these evolving convective processes.

Figures S3-S5 show daily accumulated total surface precipitation from BASE, ESTAR, and PRISM for June 15–18, along with corresponding WRF–PRISM differences.

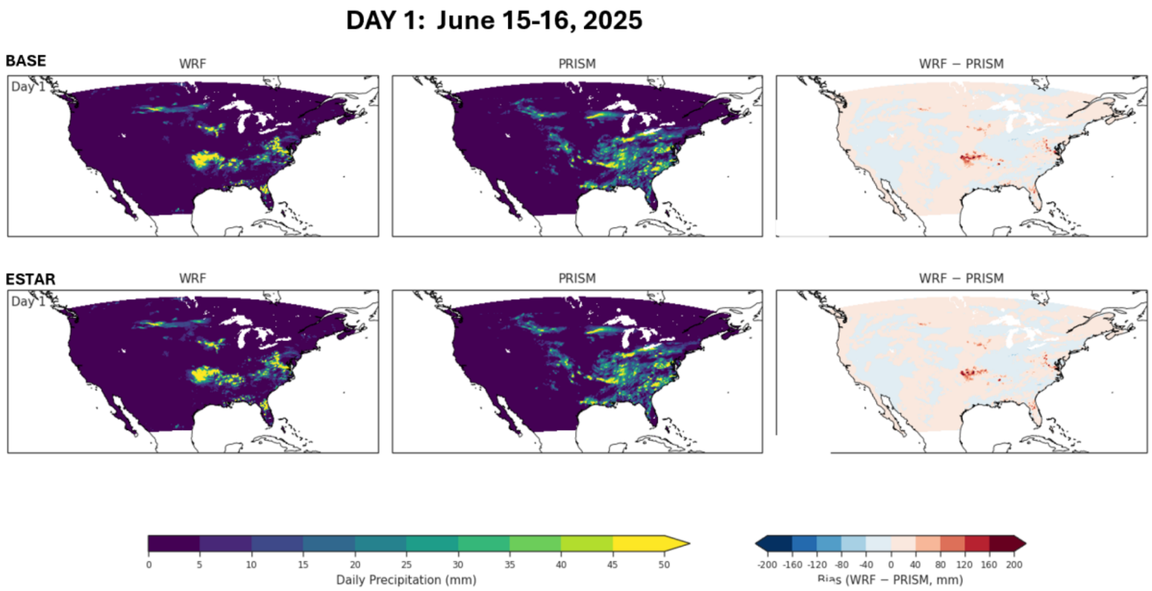

Figure S3. Daily accumulated total surface precipitation for Day 1 from BASE, ESTAR, and PRISM for June 15–16, along with corresponding WRF–PRISM differences.

For Day 1 (June 15–16) shown above, both BASE and ESTAR capture the broad spatial distribution of precipitation across the central, Midwestern, and eastern United States. Peak daily accumulations in the model and PRISM are generally in the range of approximately 30–50 mm. However, BASE exhibits localized strong positive biases of approximately +40 to +120 mm over parts of the central Plains and Midwest, accompanied by surrounding negative biases of approximately −20 to −60 mm. This pattern indicates both over-intensification and spatial displacement of convection. ESTAR reduces the magnitude of these extremes, with positive biases generally closer to +20 to +80 mm and negative biases closer to −20 to −40 mm. The ESTAR precipitation field is therefore less concentrated and more spatially balanced than BASE.

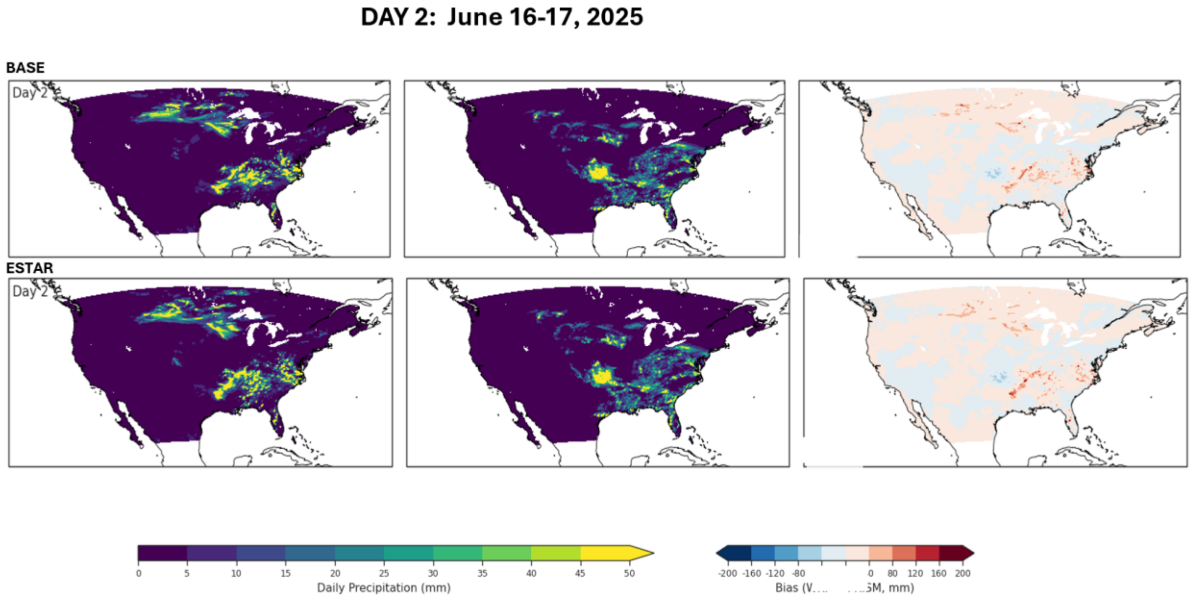

Figure S4. Daily accumulated total surface precipitation for Day 2 from BASE, ESTAR, and PRISM for June 16–17, along with corresponding WRF–PRISM differences.

For Day 2 (June 16–17) shown above, BASE again shows moderate to strong positive precipitation biases, with localized values of approximately +30 to +100 mm, along with widespread negative biases of −20 to −60 mm. These errors indicate displacement and uneven distribution of convective rainfall. ESTAR produces less intense and more spatially distributed precipitation, with biases generally confined to approximately +20 to +80 mm and −20 to −40 mm.

For Day 3 (June 17–18) shown below, BASE displays widespread moderate to strong positive biases across parts of the eastern United States, again reaching approximately +40 to +120 mm in localized regions. ESTAR reduces these excessive positive biases to approximately +20 to +80 mm and also moderates negative biases to roughly −20 to −40 mm. The daily results therefore show a consistent pattern: ESTAR reduces extreme precipitation biases and produces less spatially concentrated rainfall maxima, while persistent spatial displacement errors remain in both simulations.

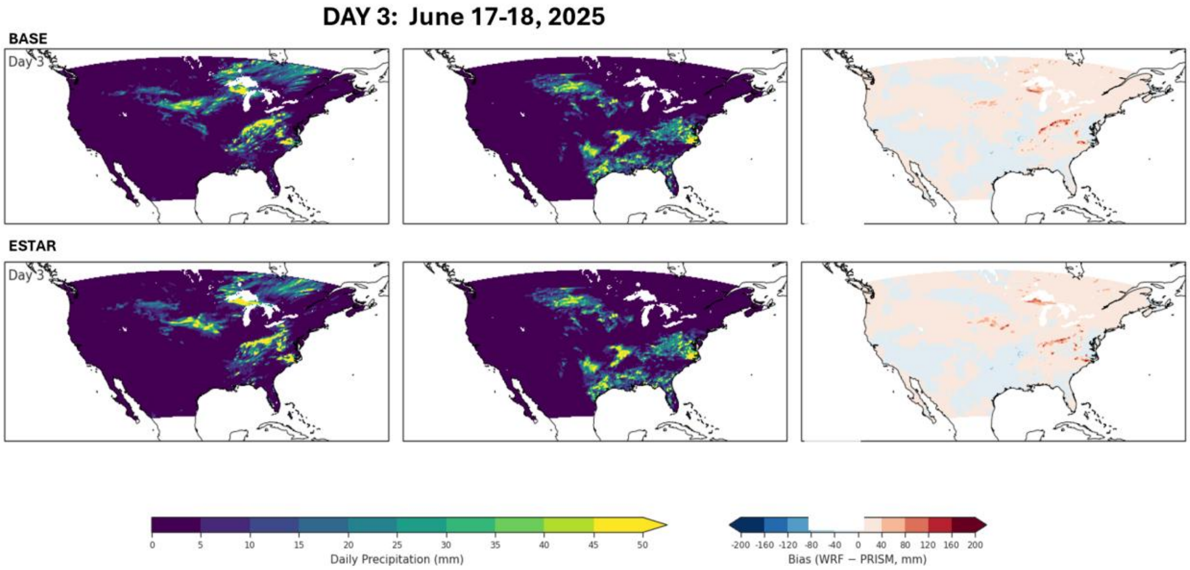

Figure S5. Daily accumulated total surface precipitation for Day 3 from BASE, ESTAR, and PRISM for June 17–18, along with corresponding WRF–PRISM differences.

Analysis of surface fields for each land use category

Since Eq. 6 uses three constants to estimate e_* for all land use categories in the simulation domain, it is necessary to evaluate the applicability and validity of these constants across all land use categories. To that effect, we have generated results for T2, Q2, and WSPD10 biases for each of the land use category, for a total of 14 land use categories, for JAN (Figs. S6-S15) and JUN (Figs. S16-S25) cases. Due to low sampling size, we have excluded land use categories 6 (Closed Shrublands), 9 (Savannas), 15 (Snow and Ice), and 16 (Barren/Sparsely Vegetated). These classes are not necessarily unimportant physically, but they are not be used as the primary evidence for evaluating whether the Eq. 6 constants are broadly applicable. Thus, the synopsis below focuses on the higher-sample land-use categories: LU 1, 2, 4, 5, 7, 8, 10, 12, 13, and 17.

After excluding low-sample land-use classes, the land-use-specific bias analysis indicates that the three constants used in Eq. 6 provide broadly stable behavior across the major sampled land-use categories, especially for WSPD10 and, to a lesser extent, Q2. The strongest and most consistent improvement associated with ESTAR is the reduction of positive 10 m wind-speed bias. Across forests, croplands, grasslands, woody savannas, urban areas, and water, BASE frequently shows a positive WSPD10 bias of roughly +1 to +3 m s^{-1}, particularly under stable conditions. ESTAR generally reduces this bias by about 0.5–1.5 m s^{-1}, often bringing the wind-speed bias closer to zero. This improvement is especially evident over croplands (LU 12), grasslands (LU 10), mixed forest (LU 5), deciduous broadleaf forest (LU 4), evergreen needleleaf forest (LU 1), and urban/built-up areas (LU 13). The reduction is not perfect, and residual positive wind bias remains over several categories, especially woody savannas (LU 8) and water (LU 17), but the overall direction of the WSPD10 response is favorable.

For Q2, most of higher-sample land-use categories show relatively small biases compared with T2 and WSPD10. In January, Q2 biases are generally within about ±0.5 to ±1.5 g kg^{-1}, with occasional larger excursions. In June, Q2 variability becomes larger over vegetated surfaces, especially deciduous broadleaf forest, mixed forest, grasslands, and croplands, where moist-bias excursions can locally approach 2–5 g kg^{-1} in some periods. Urban areas often show weaker or slightly dry Q2 behavior during unstable summer periods, consistent with limited surface moisture availability. Overall, ESTAR and BASE are often close in Q2, indicating that moisture bias is controlled not only by surface-layer exchange but also by land-surface moisture availability, vegetation state, and synoptic evolution.

For T2, the behavior is more land-use and season dependent. ESTAR does not produce a uniform temperature improvement across categories. In JAN, several forested categories show persistent cool biases, especially deciduous broadleaf forest (LU 4) and mixed forest (LU 5), where T2 biases frequently reach about −0.5 to −1 K, particularly under unstable conditions. Croplands (LU 12) also show a cool tendency in JAN, generally around −0.1 to −1 K. Urban/built-up areas (LU 13) and water (LU 17) show similar behavior. In JUN, both BASE and ESTAR has a warm bias over many vegetated surfaces, especially croplands, grasslands, mixed forest, deciduous broadleaf forest, woody savannas, and urban areas, with common excursions of about +1 to +4 K; however, both BASE and ESTAR follow closely each other. The land-use-dependent T2 response in ESTAR can also be interpreted in the context of the present hybrid implementation. Although ESTAR removes explicit similarity functions from the surface-layer exchange formulation, the host PBL scheme still retains similarity-based assumptions in its treatment of vertical mixing and stability-dependent turbulence. This creates a potential inconsistency between the similarity function-free surface-layer physics and the MOST-dependent PBL response. Such inconsistency is expected to affect T2 more strongly than WSPD10, because near-surface temperature depends on the coupled evolution of sensible heat flux, skin temperature, ground heat storage, and PBL depth. Therefore, the remaining ESTAR small T2 biases do not necessarily indicate an issue with the ESTAR constants, but rather point to the need for a fully consistent MOST–free surface–PBL framework, which will be addressed in a future study. Overall, after excluding low-sample categories, the results support the conclusion that the Eq. 6 constants are reasonably transferable across the dominant land-use categories, particularly for improving WSPD10.

Figures S6 to S25 are given below starting next page.

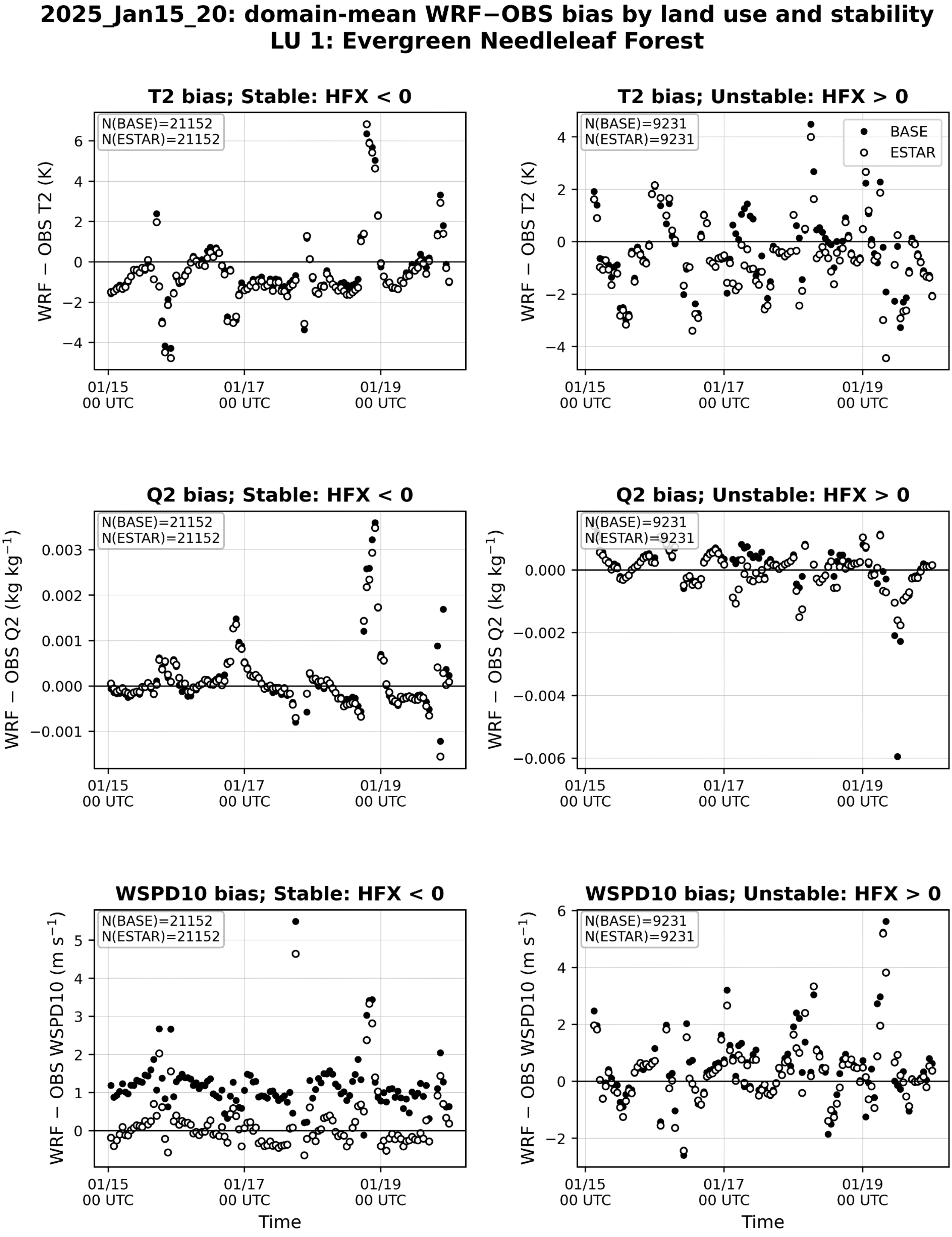
2025_Jan15_20: domain-mean WRF−OBS bias by land use and stability
LU 1: Evergreen Needleleaf Forest
T2 bias; Stable: HFX < 0
N(BASE)=21152
N(ESTAR)=21152
WRF − OBS T2 (K)
T2 bias; Unstable: HFX > 0
N(BASE)=9231
N(ESTAR)=9231
BASE
ESTAR
Q2 bias; Stable: HFX < 0
WRF − OBS Q2 (kg kg^{-1})
Q2 bias; Unstable: HFX > 0
WSPD10 bias; Stable: HFX < 0
WRF − OBS WSPD10 (m s^{-1})
WSPD10 bias; Unstable: HFX > 0
01/15 00 UTC
01/17 00 UTC
01/19 00 UTC
Time

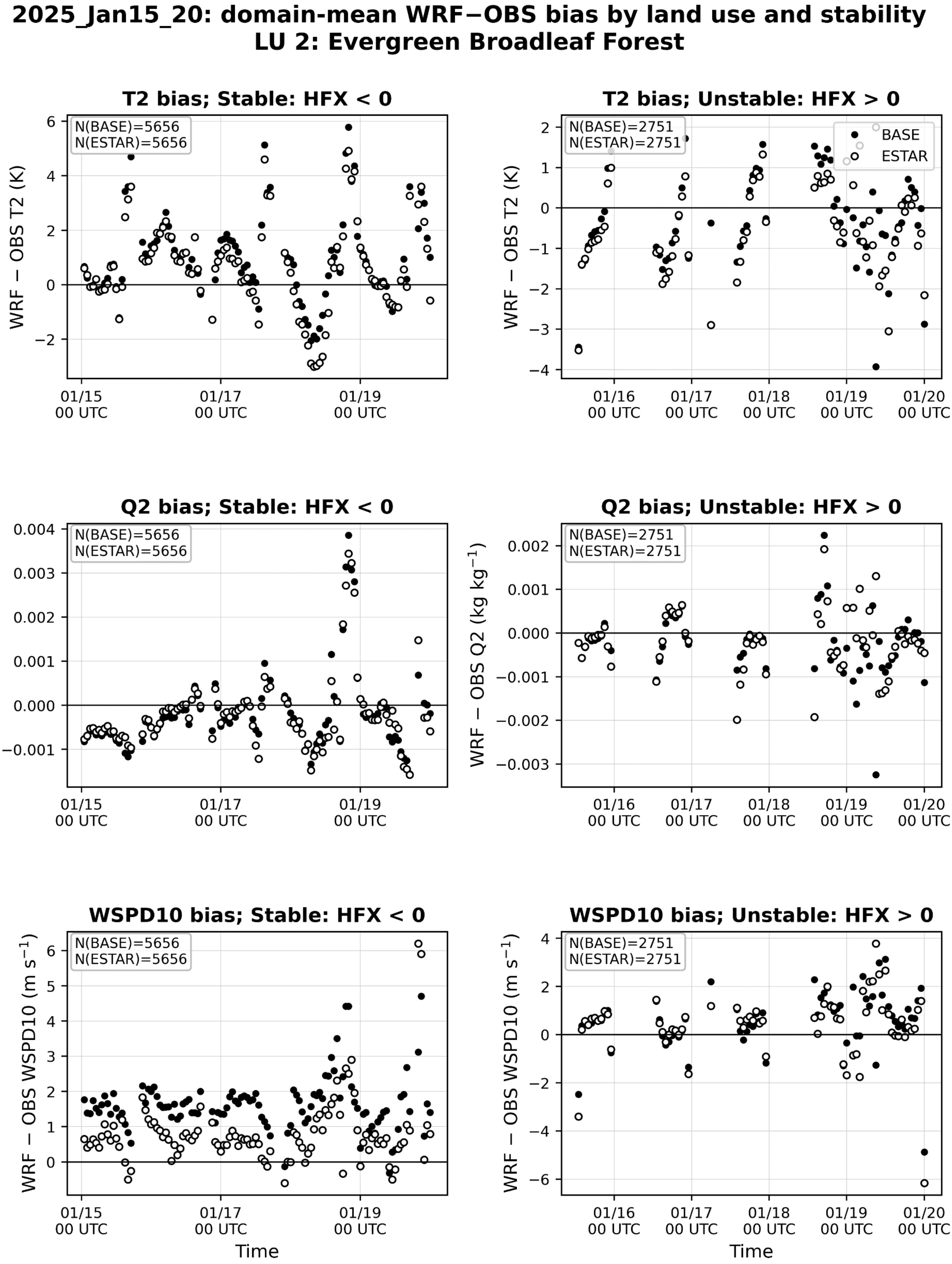
2025_Jan15_20: domain-mean WRF−OBS bias by land use and stability
LU 2: Evergreen Broadleaf Forest
T2 bias; Stable: HFX < 0
N(BASE)=5656
N(ESTAR)=5656
WRF − OBS T2 (K)
T2 bias; Unstable: HFX > 0
N(BASE)=2751
N(ESTAR)=2751
BASE
ESTAR
Q2 bias; Stable: HFX < 0
WRF − OBS Q2 (kg kg⁻¹)
Q2 bias; Unstable: HFX > 0
WSPD10 bias; Stable: HFX < 0
WRF − OBS WSPD10 (m s⁻¹)
WSPD10 bias; Unstable: HFX > 0
01/15 00 UTC
01/16 00 UTC
01/17 00 UTC
01/18 00 UTC
01/19 00 UTC
01/20 00 UTC
Time

2025_Jan15_20: domain-mean WRF−OBS bias by land use and stability
LU 4: Deciduous Broadleaf Forest

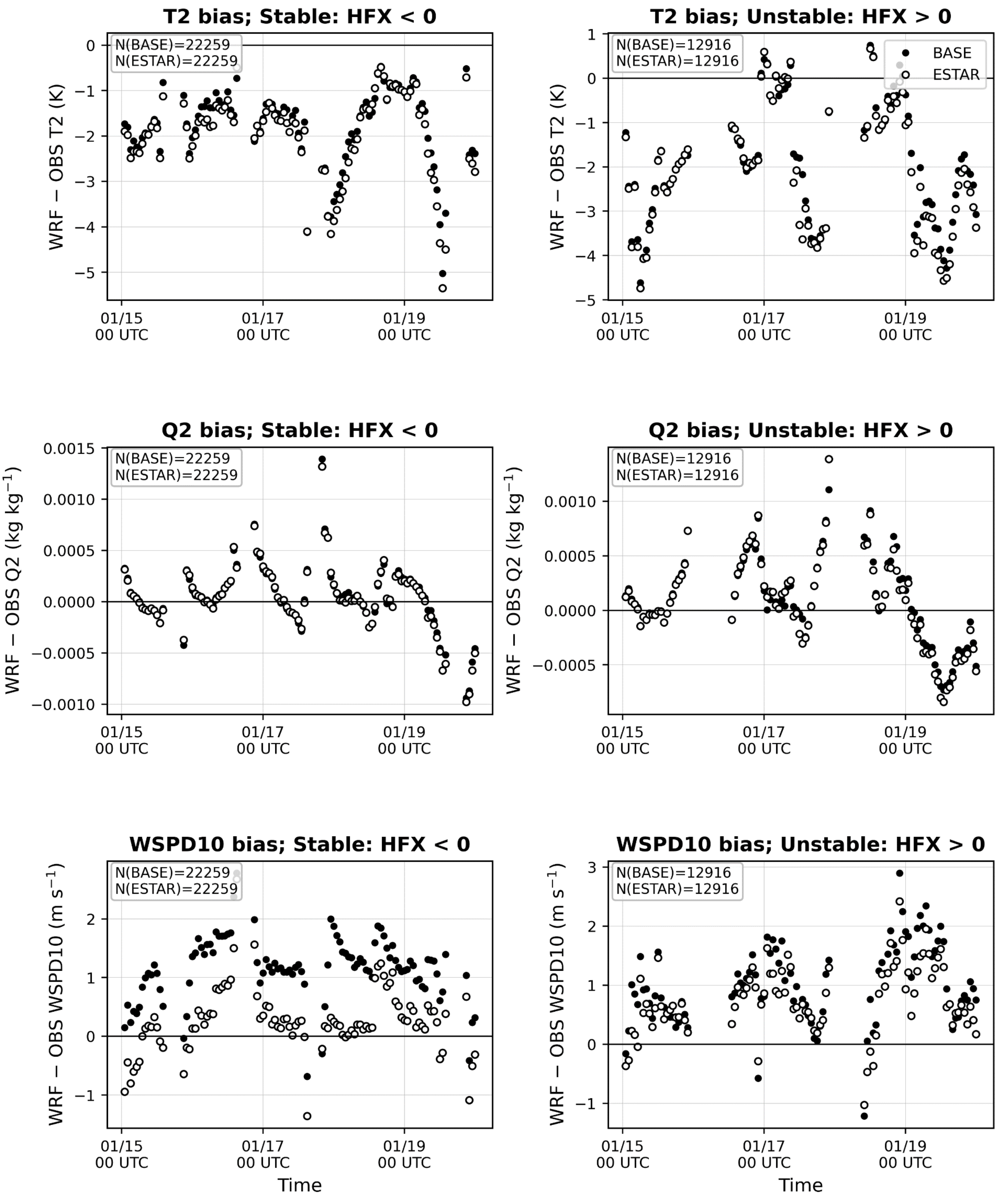

2025_Jan15_20: domain-mean WRF−OBS bias by land use and stability
LU 5: Mixed Forest

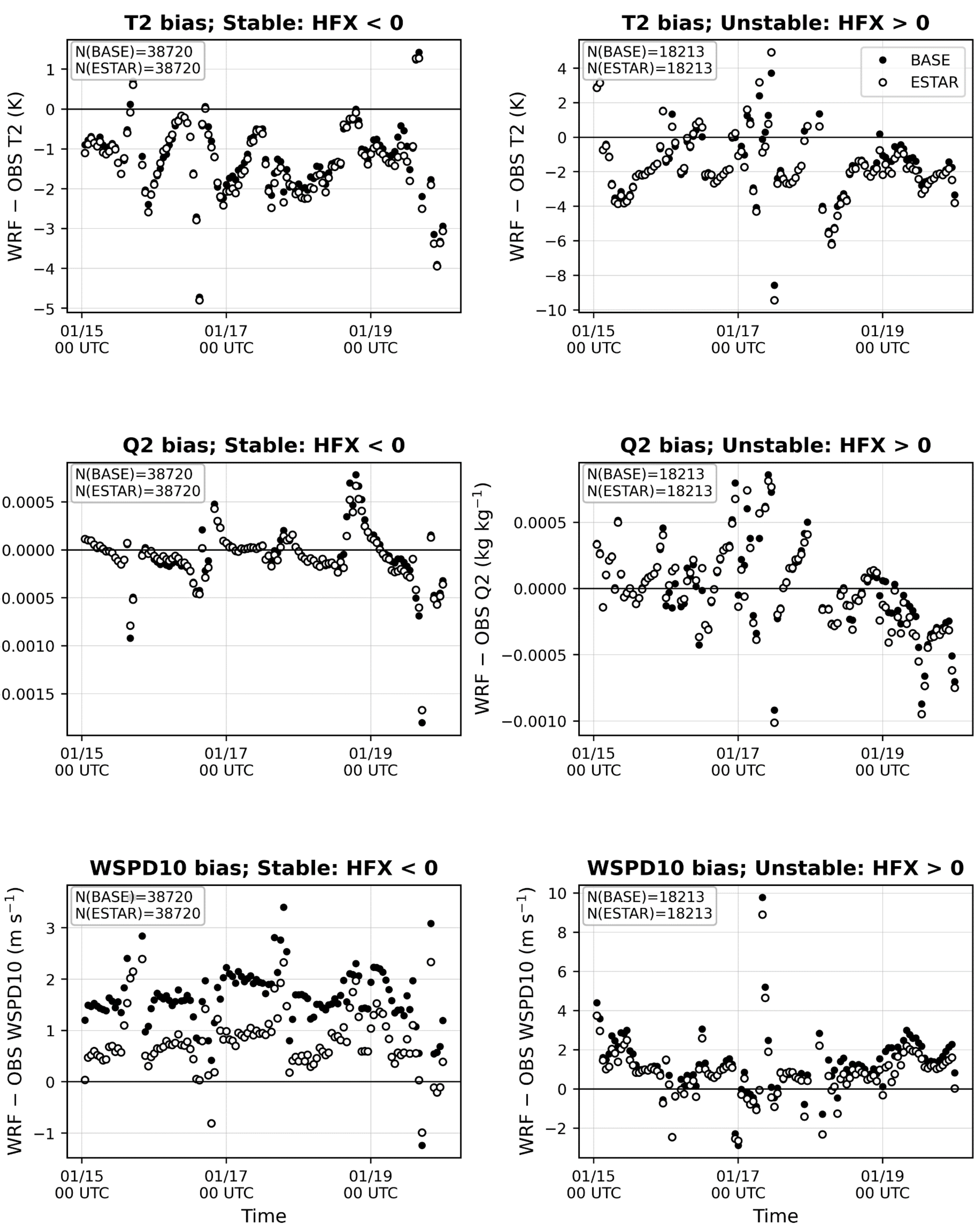

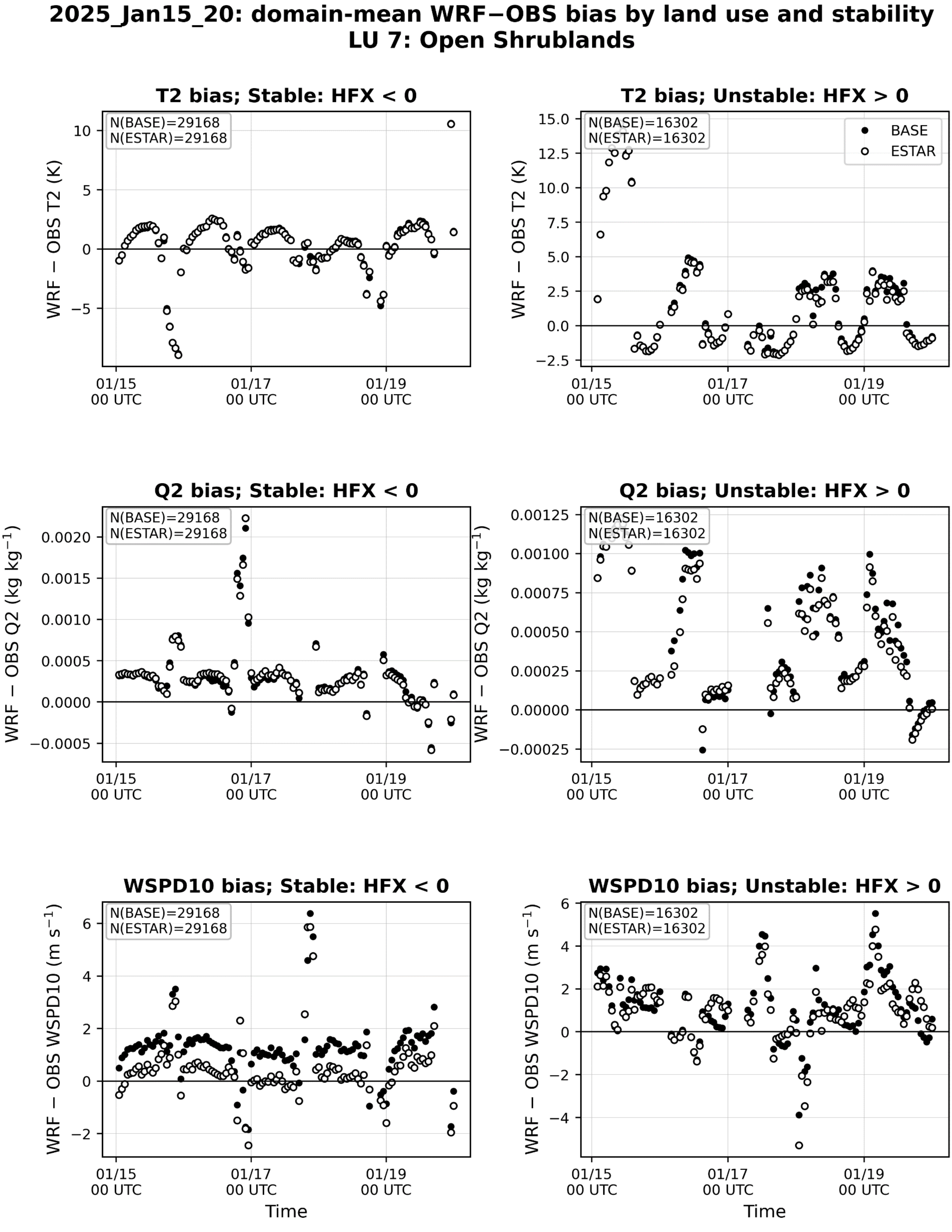
2025_Jan15_20: domain-mean WRF−OBS bias by land use and stability
LU 7: Open Shrublands
T2 bias; Stable: HFX < 0
N(BASE)=29168
N(ESTAR)=29168
WRF − OBS T2 (K)
T2 bias; Unstable: HFX > 0
N(BASE)=16302
N(ESTAR)=16302
BASE
ESTAR
WRF − OBS T2 (K)
Q2 bias; Stable: HFX < 0
N(BASE)=29168
N(ESTAR)=29168
WRF − OBS Q2 (kg kg^{-1})
Q2 bias; Unstable: HFX > 0
N(BASE)=16302
N(ESTAR)=16302
WRF − OBS Q2 (kg kg^{-1})
WSPD10 bias; Stable: HFX < 0
N(BASE)=29168
N(ESTAR)=29168
WRF − OBS WSPD10 (m s^{-1})
WSPD10 bias; Unstable: HFX > 0
N(BASE)=16302
N(ESTAR)=16302
WRF − OBS WSPD10 (m s^{-1})
01/15 00 UTC
01/17 00 UTC
01/19 00 UTC
Time

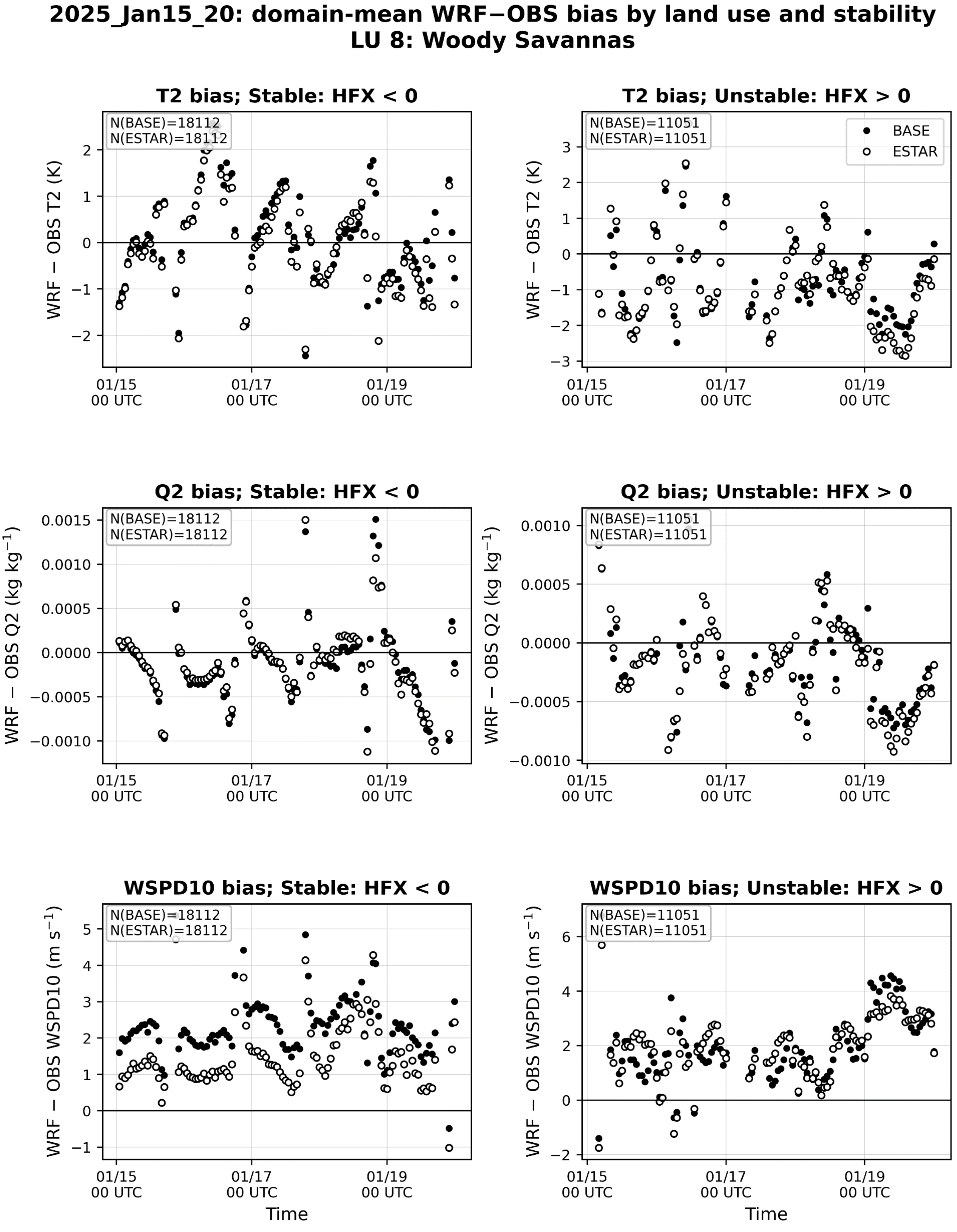
2025_Jan15_20: domain-mean WRF−OBS bias by land use and stability
LU 8: Woody Savannas
T2 bias; Stable: HFX < 0
N(BASE)=18112
N(ESTAR)=18112
WRF − OBS T2 (K)
T2 bias; Unstable: HFX > 0
N(BASE)=11051
N(ESTAR)=11051
BASE
ESTAR
Q2 bias; Stable: HFX < 0
WRF − OBS Q2 (kg kg^{-1})
Q2 bias; Unstable: HFX > 0
WSPD10 bias; Stable: HFX < 0
WRF − OBS WSPD10 (m s^{-1})
WSPD10 bias; Unstable: HFX > 0
01/15 00 UTC
01/17 00 UTC
01/19 00 UTC
Time

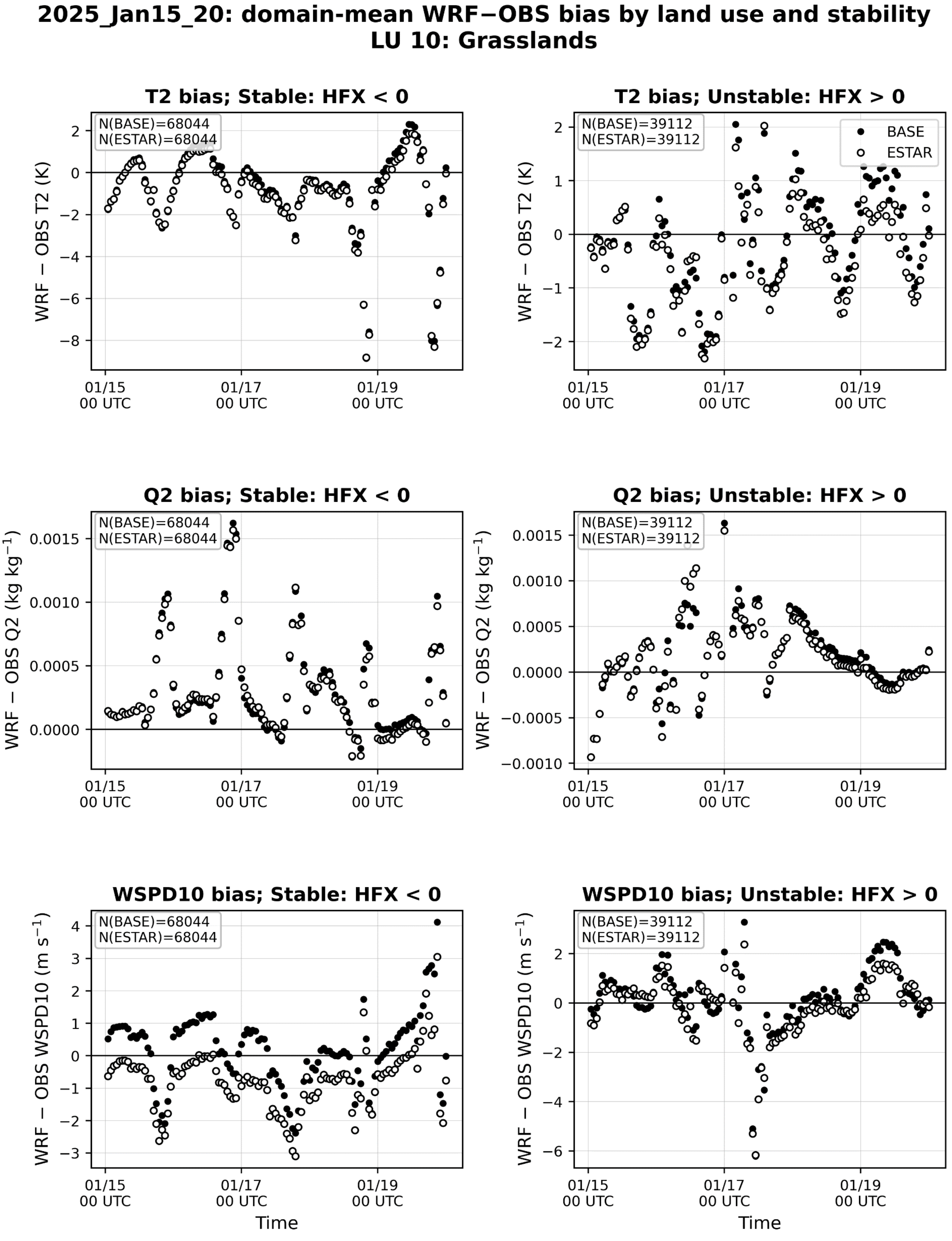

2025_Jan15_20: domain-mean WRF−OBS bias by land use and stability
LU 10: Grasslands
T2 bias; Stable: HFX < 0
N(BASE)=68044
N(ESTAR)=68044
WRF − OBS T2 (K)
T2 bias; Unstable: HFX > 0
N(BASE)=39112
N(ESTAR)=39112
BASE
ESTAR
Q2 bias; Stable: HFX < 0
N(BASE)=68044
N(ESTAR)=68044
WRF − OBS Q2 (kg kg⁻¹)
Q2 bias; Unstable: HFX > 0
N(BASE)=39112
N(ESTAR)=39112
WSPD10 bias; Stable: HFX < 0
N(BASE)=68044
N(ESTAR)=68044
WRF − OBS WSPD10 (m s⁻¹)
WSPD10 bias; Unstable: HFX > 0
N(BASE)=39112
N(ESTAR)=39112
01/15 00 UTC
01/17 00 UTC
01/19 00 UTC
Time

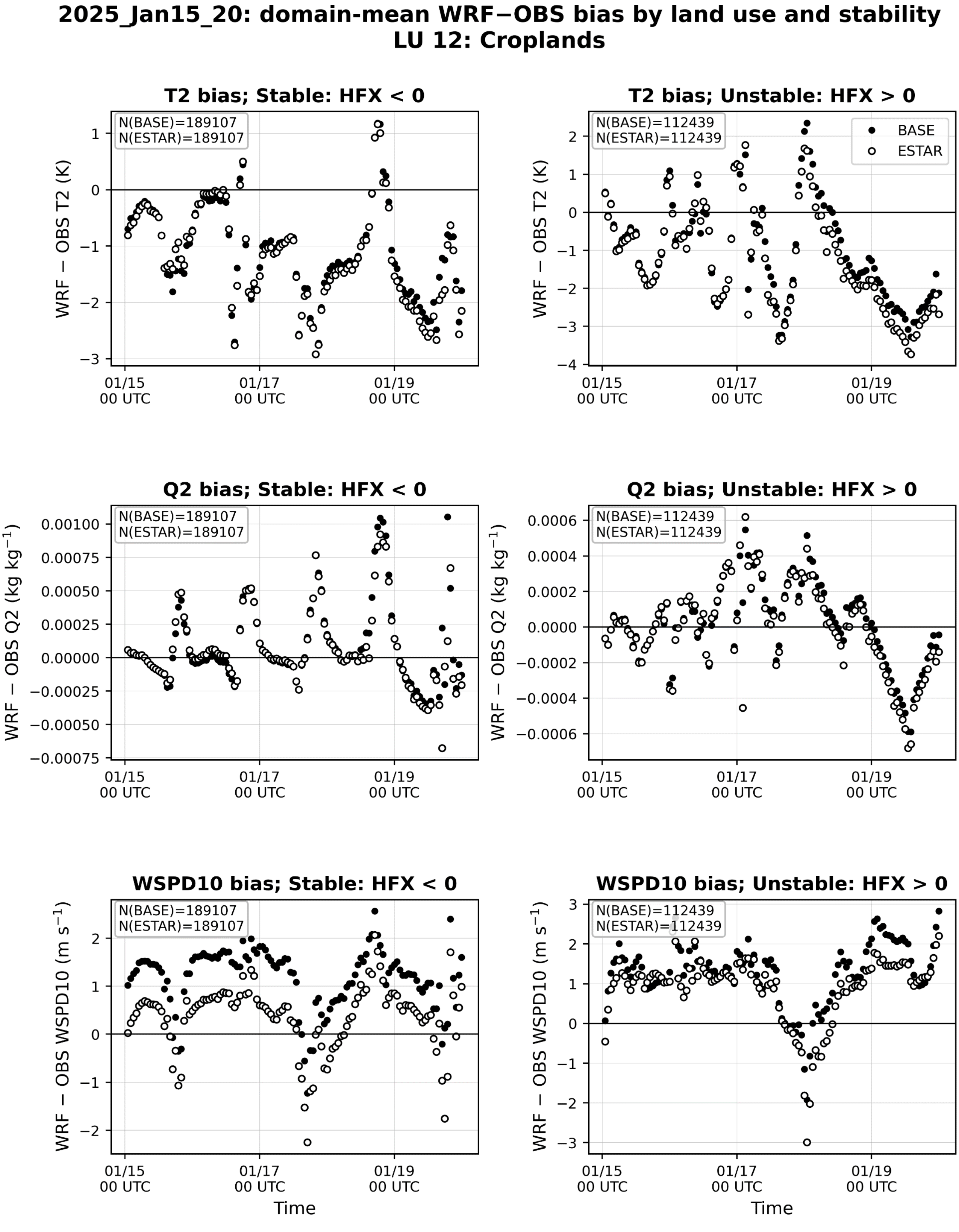
2025_Jan15_20: domain-mean WRF−OBS bias by land use and stability
LU 12: Croplands
T2 bias; Stable: HFX < 0
N(BASE)=189107
N(ESTAR)=189107
WRF − OBS T2 (K)
T2 bias; Unstable: HFX > 0
N(BASE)=112439
N(ESTAR)=112439
BASE
ESTAR
Q2 bias; Stable: HFX < 0
WRF − OBS Q2 (kg kg−1)
Q2 bias; Unstable: HFX > 0
WSPD10 bias; Stable: HFX < 0
WRF − OBS WSPD10 (m s−1)
WSPD10 bias; Unstable: HFX > 0
01/15 00 UTC
01/17 00 UTC
01/19 00 UTC
Time

2025_Jan15_20: domain-mean WRF−OBS bias by land use and stability
LU 13: Urban and Built-Up

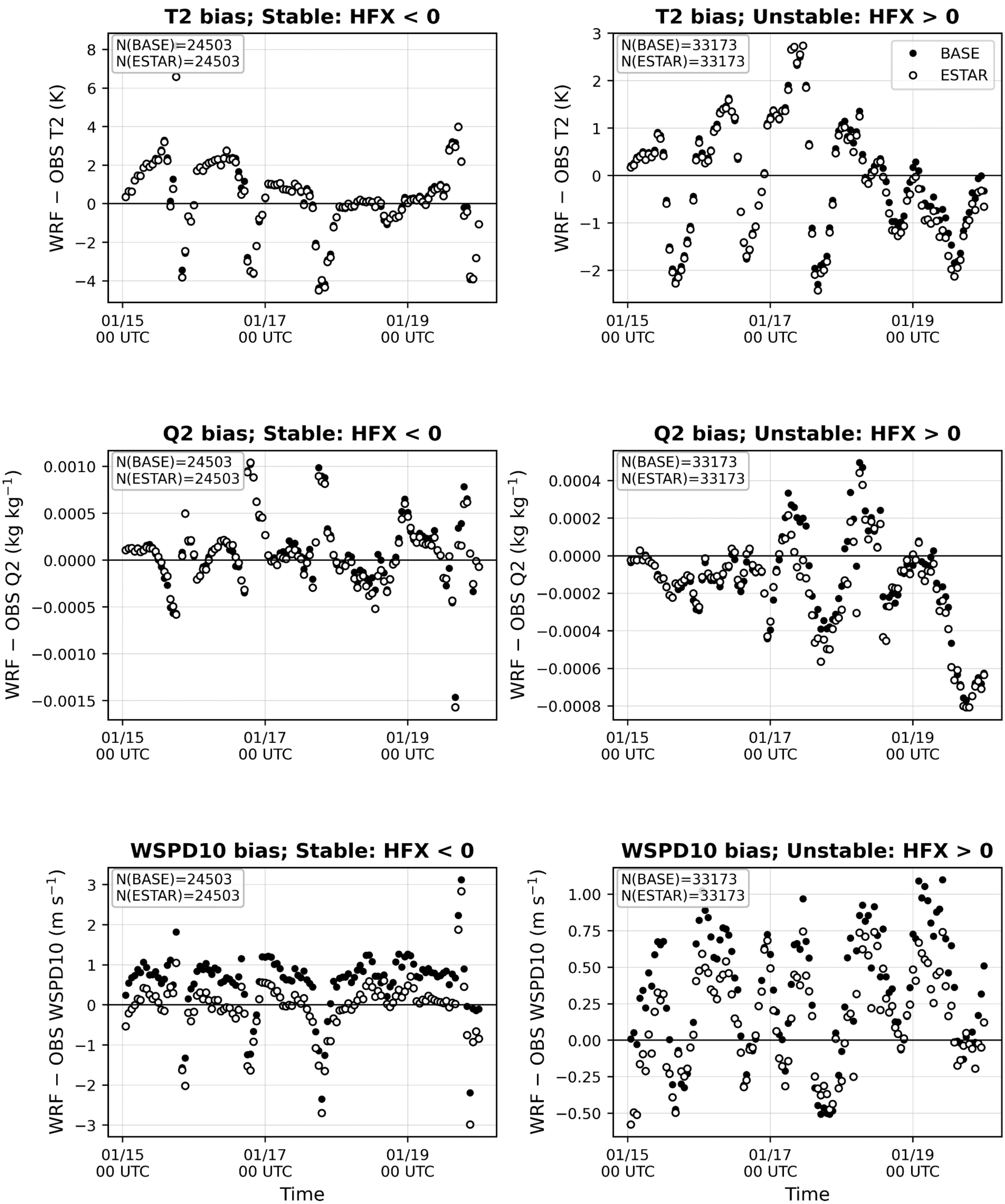

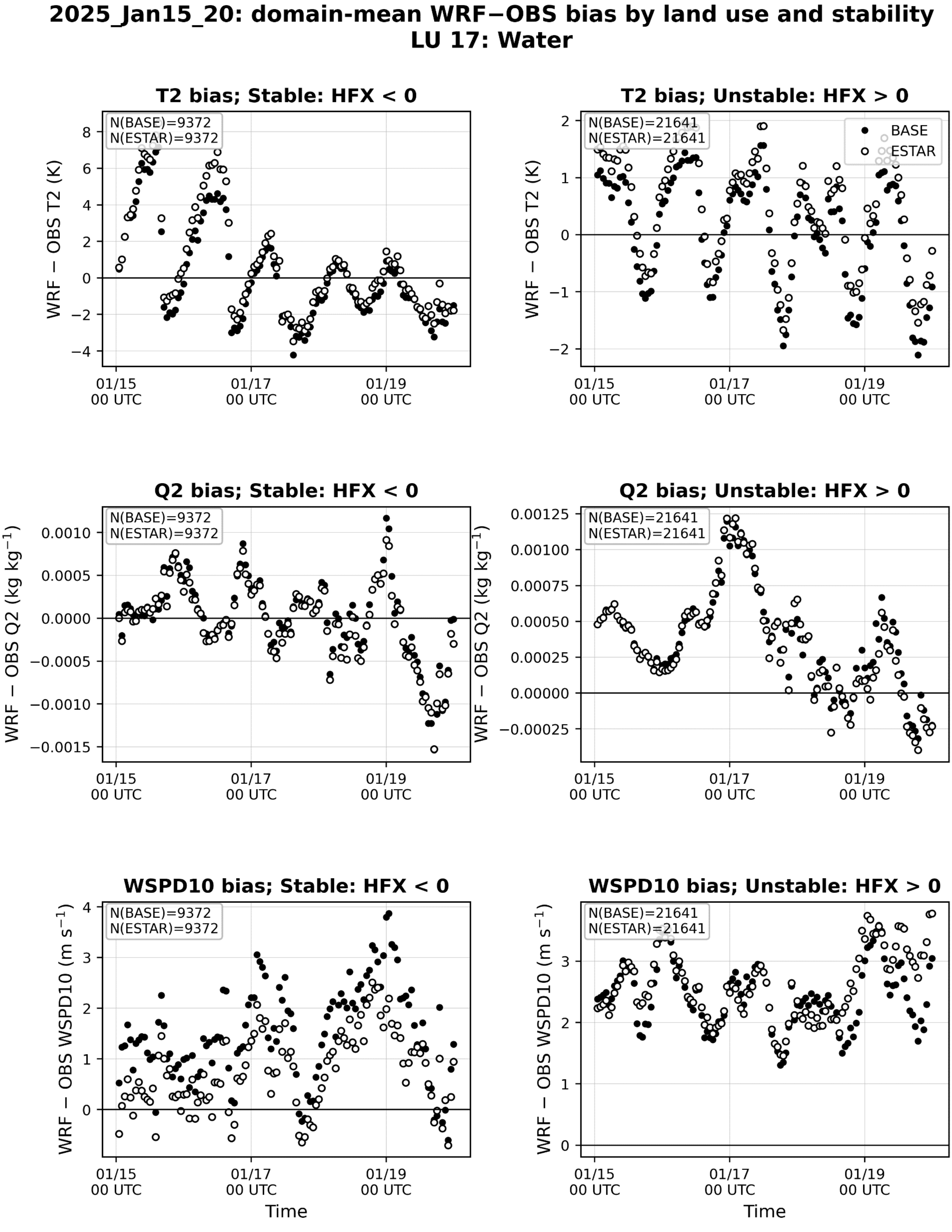
2025_Jan15_20: domain-mean WRF−OBS bias by land use and stability
LU 17: Water
T2 bias; Stable: HFX < 0
N(BASE)=9372
N(ESTAR)=9372
WRF − OBS T2 (K)
T2 bias; Unstable: HFX > 0
N(BASE)=21641
N(ESTAR)=21641
BASE
ESTAR
Q2 bias; Stable: HFX < 0
N(BASE)=9372
N(ESTAR)=9372
WRF − OBS Q2 (kg kg⁻¹)
Q2 bias; Unstable: HFX > 0
N(BASE)=21641
N(ESTAR)=21641
WSPD10 bias; Stable: HFX < 0
N(BASE)=9372
N(ESTAR)=9372
WRF − OBS WSPD10 (m s⁻¹)
WSPD10 bias; Unstable: HFX > 0
N(BASE)=21641
N(ESTAR)=21641
01/15 00 UTC
01/17 00 UTC
01/19 00 UTC
Time

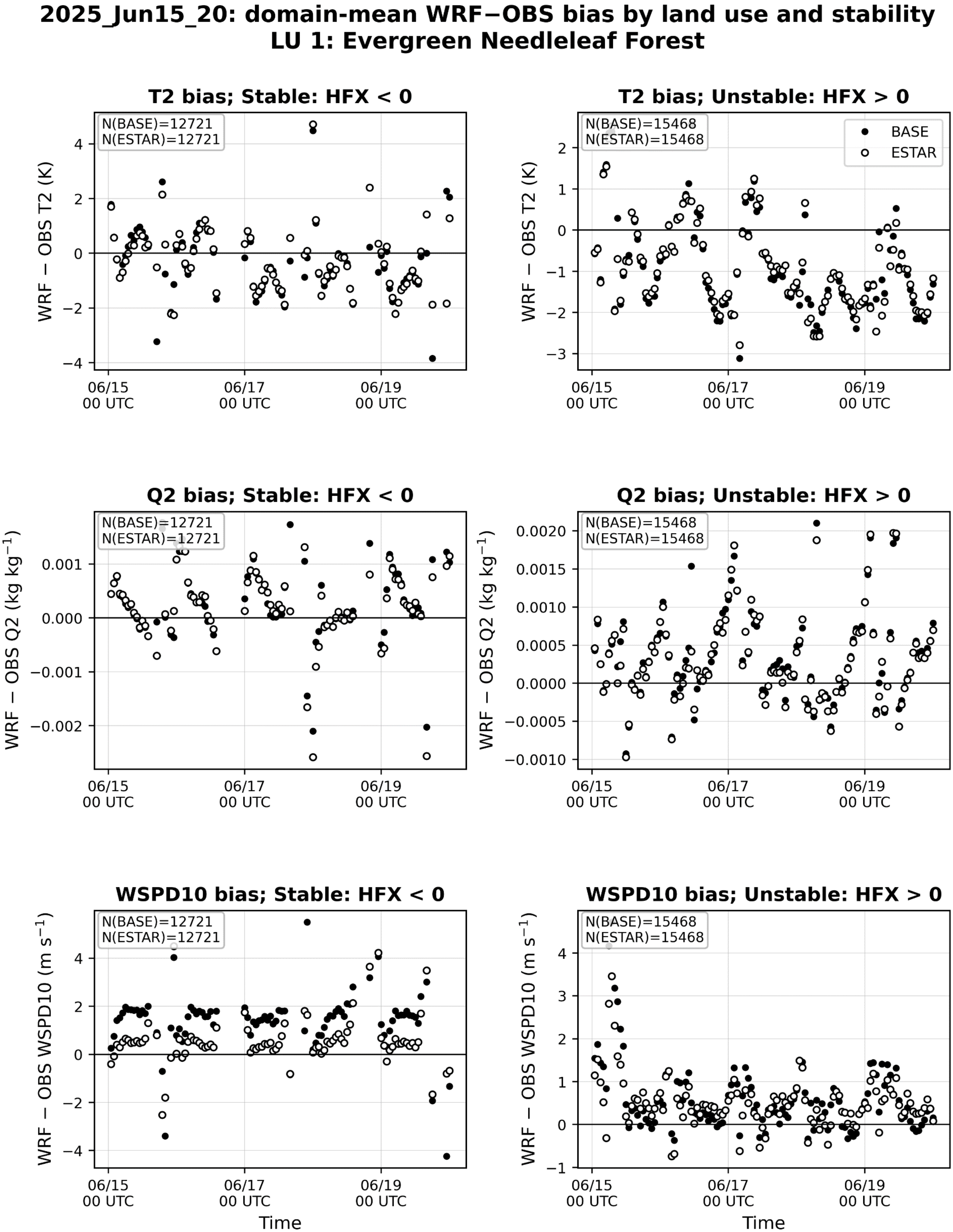
2025_Jun15_20: domain-mean WRF−OBS bias by land use and stability
LU 1: Evergreen Needleleaf Forest
T2 bias; Stable: HFX < 0
T2 bias; Unstable: HFX > 0
Q2 bias; Stable: HFX < 0
Q2 bias; Unstable: HFX > 0
WSPD10 bias; Stable: HFX < 0
WSPD10 bias; Unstable: HFX > 0
N(BASE)=12721
N(ESTAR)=12721
N(BASE)=15468
N(ESTAR)=15468
BASE
ESTAR
WRF − OBS T2 (K)
WRF − OBS Q2 (kg kg−1)
WRF − OBS WSPD10 (m s−1)
06/15 00 UTC
06/17 00 UTC
06/19 00 UTC
Time

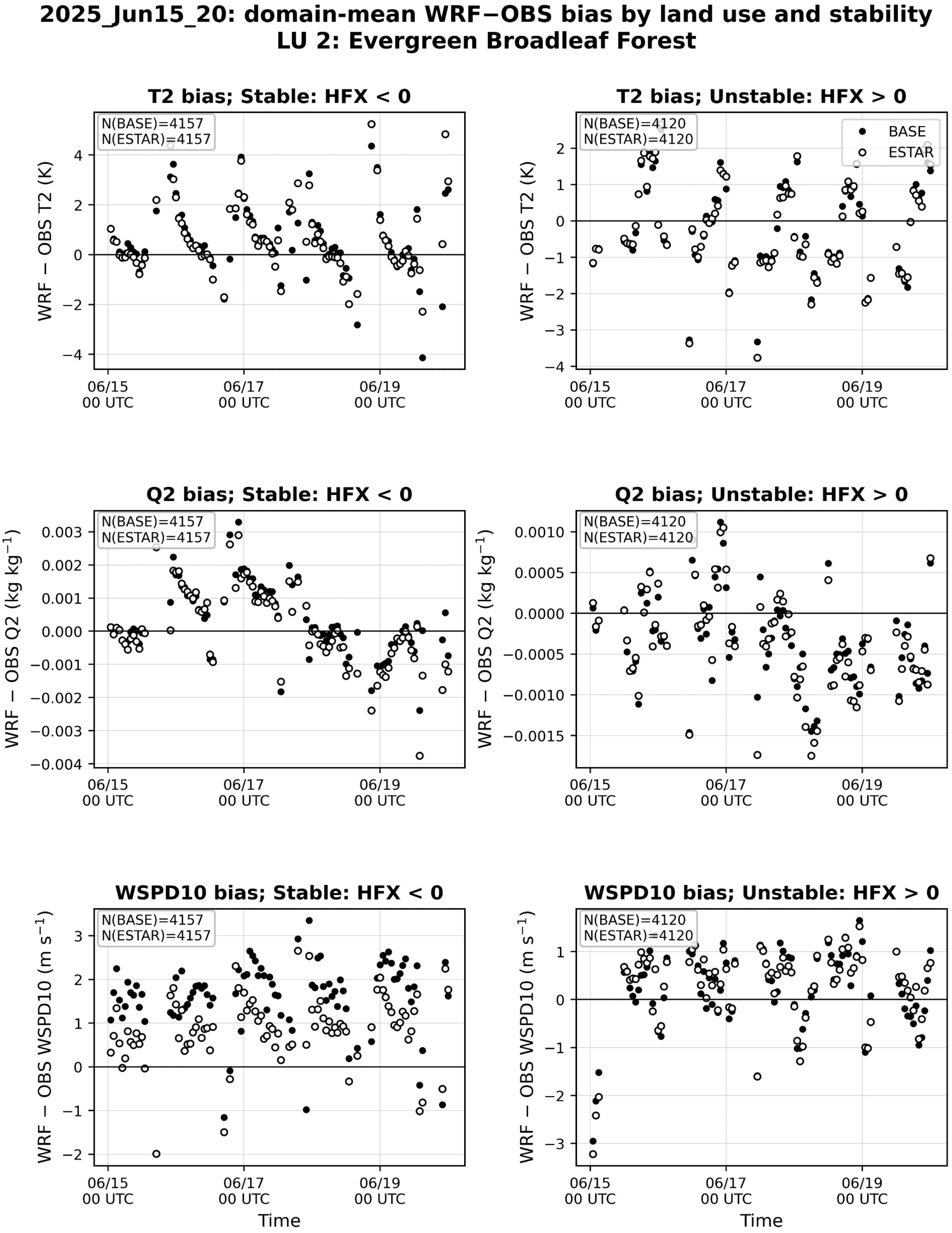
2025_Jun15_20: domain-mean WRF−OBS bias by land use and stability
LU 2: Evergreen Broadleaf Forest
T2 bias; Stable: HFX < 0
T2 bias; Unstable: HFX > 0
Q2 bias; Stable: HFX < 0
Q2 bias; Unstable: HFX > 0
WSPD10 bias; Stable: HFX < 0
WSPD10 bias; Unstable: HFX > 0
N(BASE)=4157
N(ESTAR)=4157
N(BASE)=4120
N(ESTAR)=4120
BASE
ESTAR
WRF − OBS T2 (K)
WRF − OBS Q2 (kg kg⁻¹)
WRF − OBS WSPD10 (m s⁻¹)
06/15 00 UTC
06/17 00 UTC
06/19 00 UTC
Time

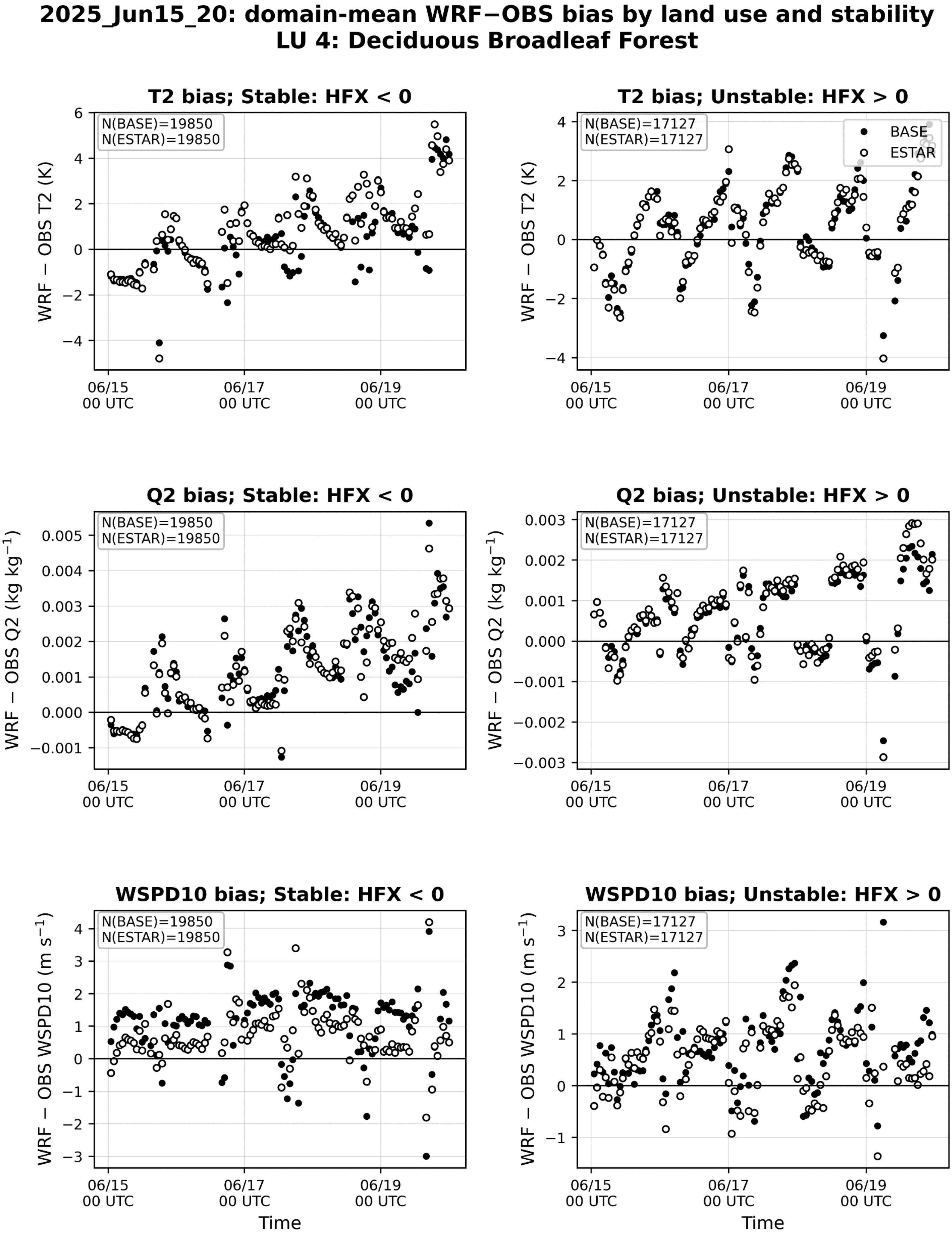

2025_Jun15_20: domain-mean WRF−OBS bias by land use and stability
LU 4: Deciduous Broadleaf Forest
T2 bias; Stable: HFX < 0
T2 bias; Unstable: HFX > 0
Q2 bias; Stable: HFX < 0
Q2 bias; Unstable: HFX > 0
WSPD10 bias; Stable: HFX < 0
WSPD10 bias; Unstable: HFX > 0
N(BASE)=19850
N(ESTAR)=19850
N(BASE)=17127
N(ESTAR)=17127
BASE
ESTAR
WRF − OBS T2 (K)
WRF − OBS Q2 (kg kg−1)
WRF − OBS WSPD10 (m s−1)
06/15 00 UTC
06/17 00 UTC
06/19 00 UTC
Time

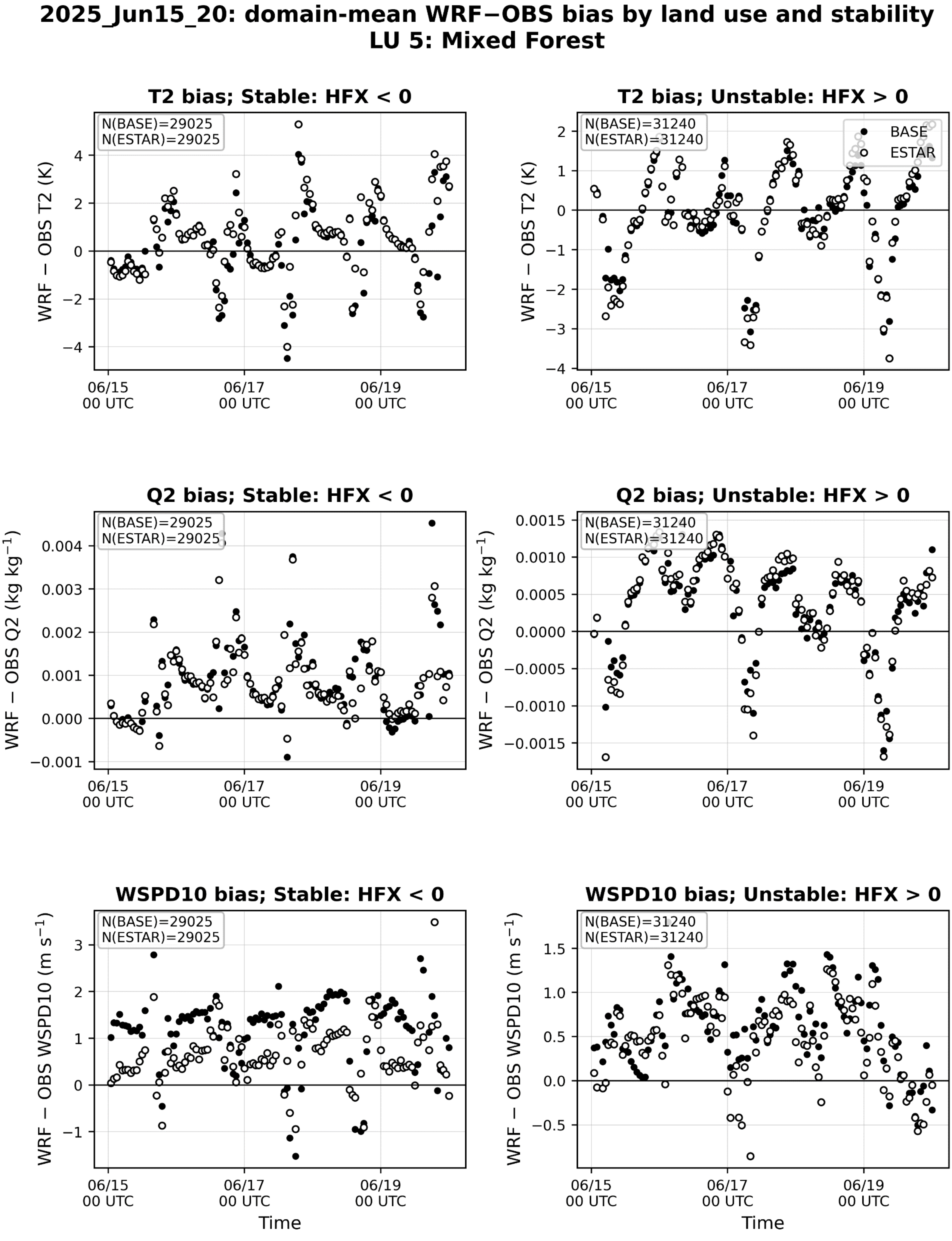
2025_Jun15_20: domain-mean WRF−OBS bias by land use and stability
LU 5: Mixed Forest
T2 bias; Stable: HFX < 0
N(BASE)=29025
N(ESTAR)=29025
WRF − OBS T2 (K)
T2 bias; Unstable: HFX > 0
N(BASE)=31240
N(ESTAR)=31240
BASE
ESTAR
Q2 bias; Stable: HFX < 0
N(BASE)=29025
N(ESTAR)=29025
WRF − OBS Q2 (kg kg−1)
Q2 bias; Unstable: HFX > 0
N(BASE)=31240
N(ESTAR)=31240
WSPD10 bias; Stable: HFX < 0
N(BASE)=29025
N(ESTAR)=29025
WRF − OBS WSPD10 (m s−1)
WSPD10 bias; Unstable: HFX > 0
N(BASE)=31240
N(ESTAR)=31240
06/15 00 UTC
06/17 00 UTC
06/19 00 UTC
Time

2025_Jun15_20: domain-mean WRF−OBS bias by land use and stability
LU 7: Open Shrublands

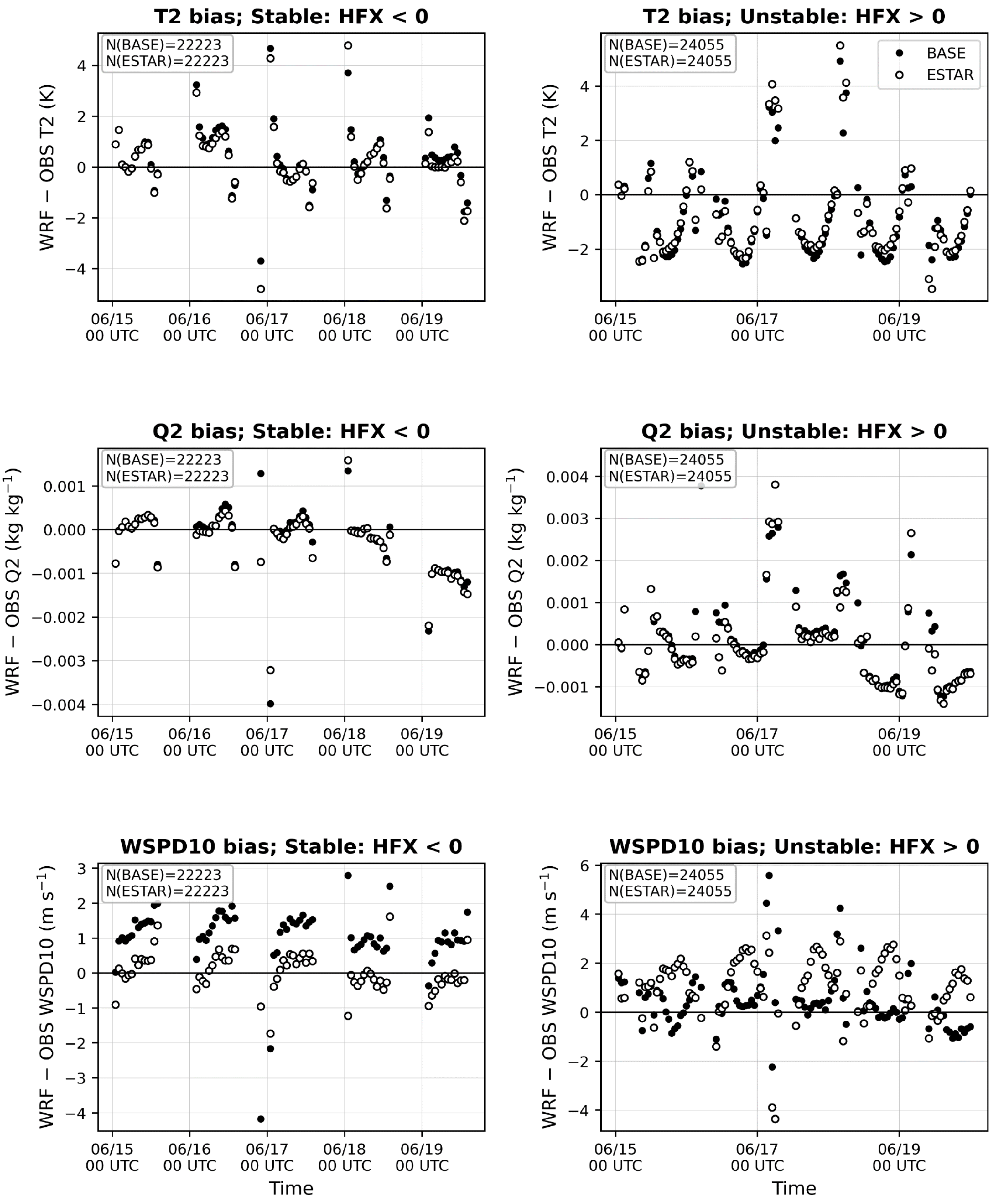

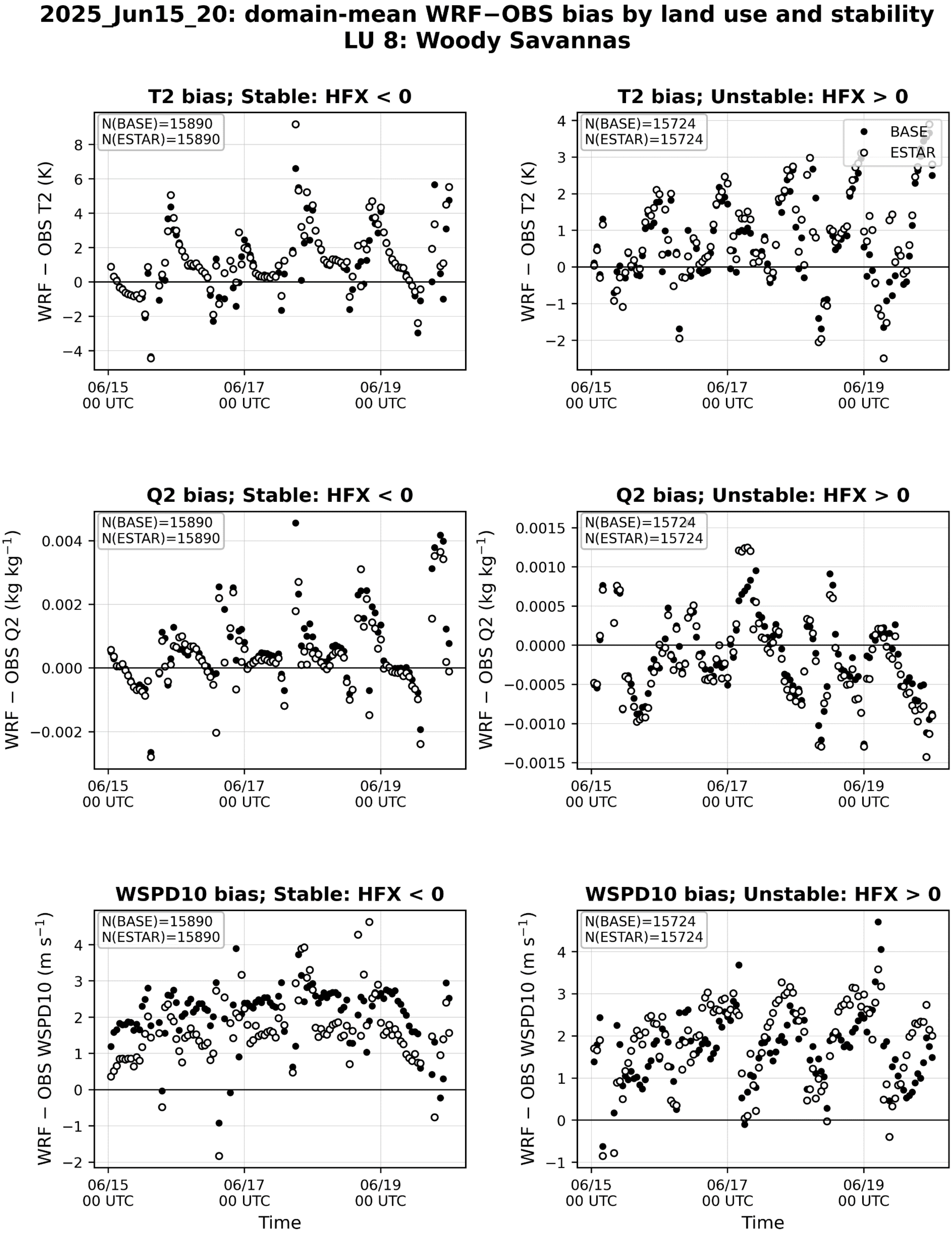

2025_Jun15_20: domain-mean WRF−OBS bias by land use and stability
LU 8: Woody Savannas
T2 bias; Stable: HFX < 0
N(BASE)=15890
N(ESTAR)=15890
WRF − OBS T2 (K)
T2 bias; Unstable: HFX > 0
N(BASE)=15724
N(ESTAR)=15724
BASE
ESTAR
Q2 bias; Stable: HFX < 0
N(BASE)=15890
N(ESTAR)=15890
WRF − OBS Q2 (kg kg^{-1})
Q2 bias; Unstable: HFX > 0
N(BASE)=15724
N(ESTAR)=15724
WSPD10 bias; Stable: HFX < 0
N(BASE)=15890
N(ESTAR)=15890
WRF − OBS WSPD10 (m s^{-1})
WSPD10 bias; Unstable: HFX > 0
N(BASE)=15724
N(ESTAR)=15724
06/15 00 UTC
06/17 00 UTC
06/19 00 UTC
Time

2025_Jun15_20: domain-mean WRF−OBS bias by land use and stability
LU 10: Grasslands

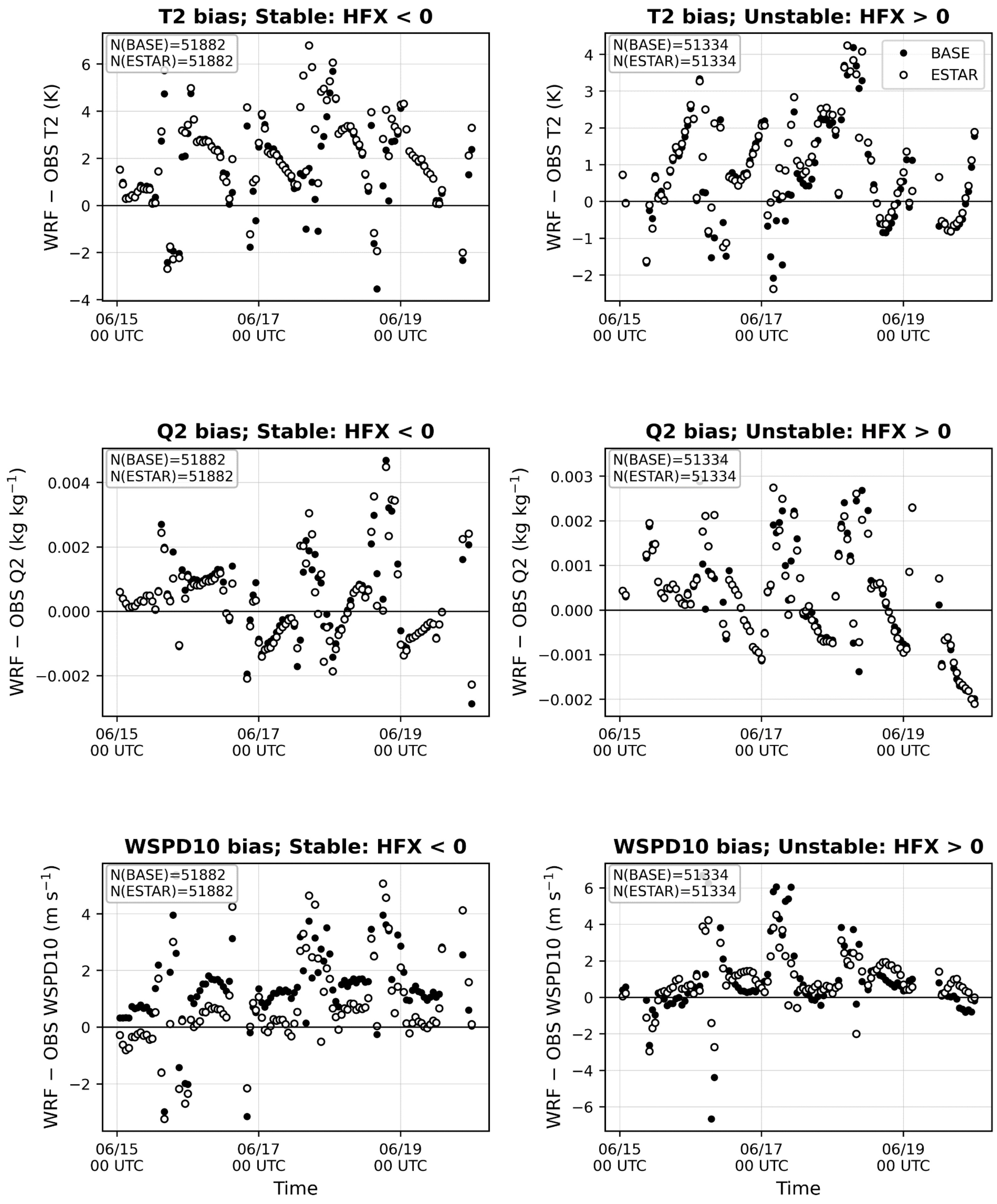

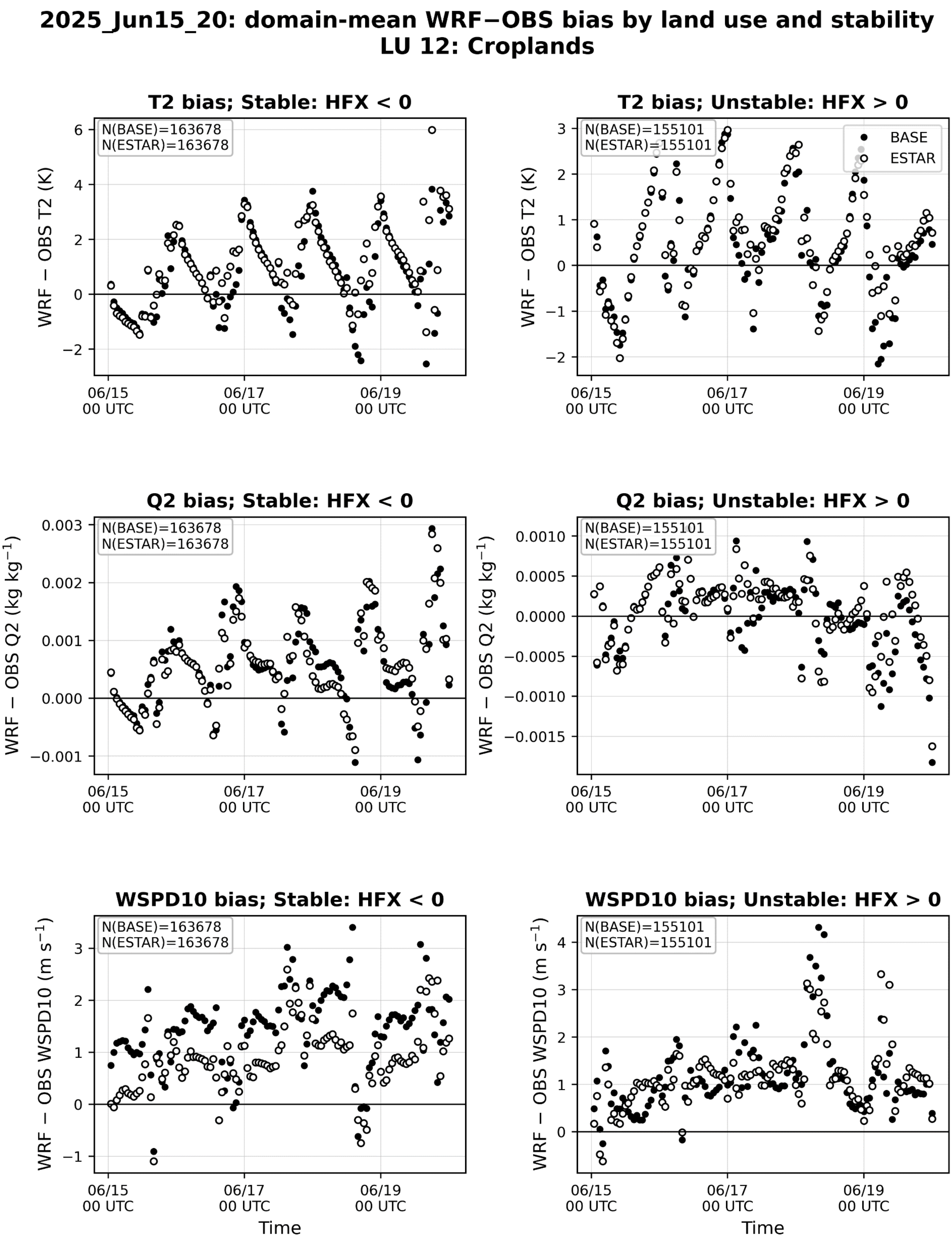
2025_Jun15_20: domain-mean WRF−OBS bias by land use and stability
LU 12: Croplands
T2 bias; Stable: HFX < 0
N(BASE)=163678
N(ESTAR)=163678
WRF − OBS T2 (K)
T2 bias; Unstable: HFX > 0
N(BASE)=155101
N(ESTAR)=155101
BASE
ESTAR
Q2 bias; Stable: HFX < 0
N(BASE)=163678
N(ESTAR)=163678
WRF − OBS Q2 (kg kg⁻¹)
Q2 bias; Unstable: HFX > 0
N(BASE)=155101
N(ESTAR)=155101
WSPD10 bias; Stable: HFX < 0
N(BASE)=163678
N(ESTAR)=163678
WRF − OBS WSPD10 (m s⁻¹)
WSPD10 bias; Unstable: HFX > 0
N(BASE)=155101
N(ESTAR)=155101
06/15 00 UTC
06/17 00 UTC
06/19 00 UTC
Time

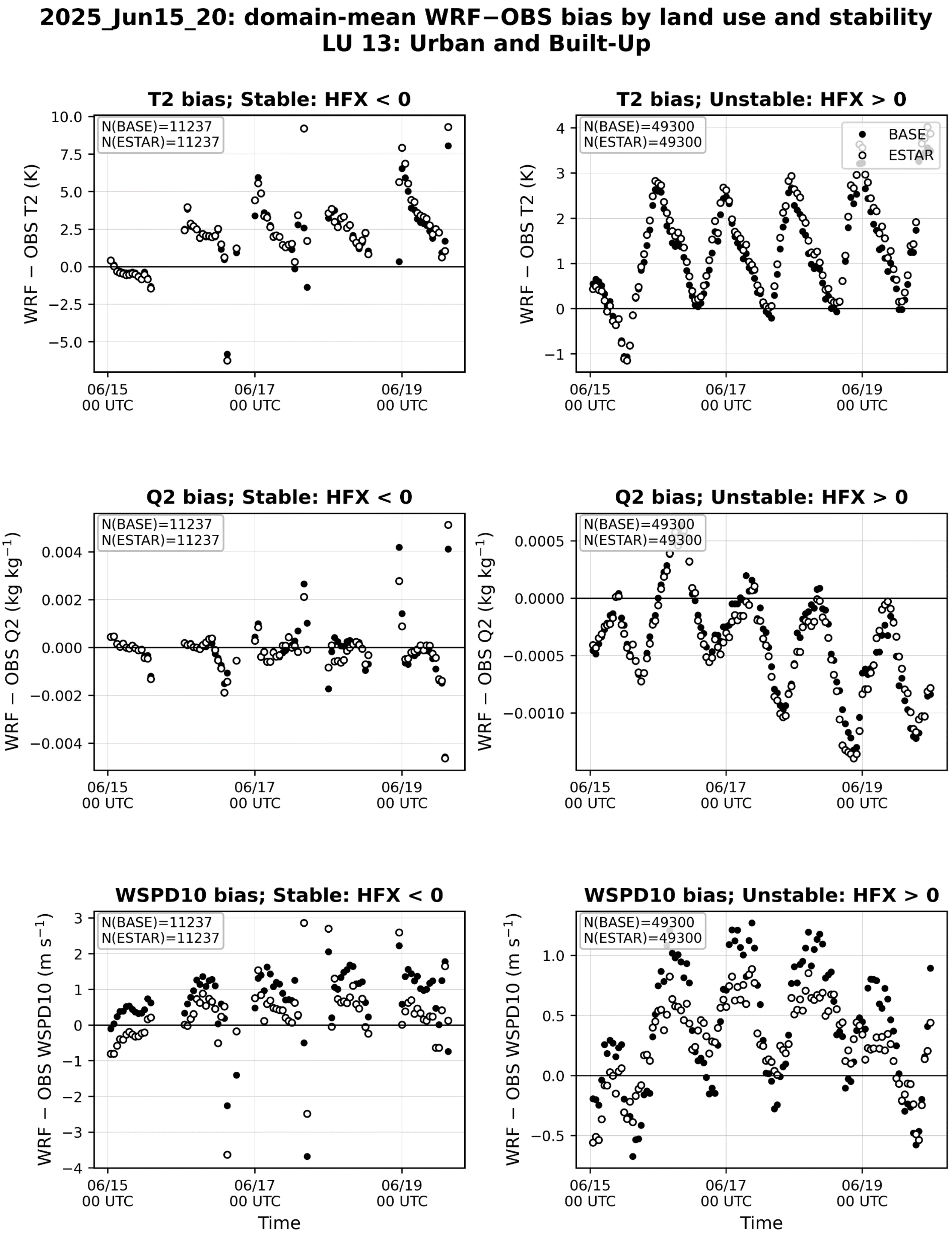
2025_Jun15_20: domain-mean WRF−OBS bias by land use and stability
LU 13: Urban and Built-Up
T2 bias; Stable: HFX < 0
N(BASE)=11237
N(ESTAR)=11237
WRF − OBS T2 (K)
T2 bias; Unstable: HFX > 0
N(BASE)=49300
N(ESTAR)=49300
BASE
ESTAR
Q2 bias; Stable: HFX < 0
N(BASE)=11237
N(ESTAR)=11237
WRF − OBS Q2 (kg kg^{-1})
Q2 bias; Unstable: HFX > 0
N(BASE)=49300
N(ESTAR)=49300
WSPD10 bias; Stable: HFX < 0
N(BASE)=11237
N(ESTAR)=11237
WRF − OBS WSPD10 (m s^{-1})
WSPD10 bias; Unstable: HFX > 0
N(BASE)=49300
N(ESTAR)=49300
06/15 00 UTC
06/17 00 UTC
06/19 00 UTC
Time

2025_Jun15_20: domain-mean WRF−OBS bias by land use and stability
LU 17: Water